**Eleventh International Conference on Computational Fluid Dynamics (ICCFD11), Maui, Hawaii, USA, July 11-15, 2022**

**ICCFD11-4204**

# Influence of Blunt-Body Base Protuberances on Near-Wake Unsteadiness

C. Stack*, L. Dechant*, B. Robbins*, Y. Zhang* and K. Casper*
Corresponding author: cstack@sandia.gov

* Sandia National Laboratories, Albuquerque, NM, USA.

**Abstract:** This work aims to assess the influence of blunt body base protuberances, such as a sting in an experiment, on near-wake unsteadiness using high-fidelity simulations. To evaluate the sensitivity of the near-wake dynamics to these geometrical features, three sting configurations are considered; a 'no-sting' case, a 'centered-sting' case (where the sting axis is aligned with the body axis), and an 'offset-sting' case (where the sting axis and body axis are offset by some distance). To generate a more comprehensive simulation database, two different types of flows are simulated, namely a Mach 2.49 cylinder wake, and a Mach 8 cone wake, thereby comprising six total cases. Flowfield visualizations highlight the influence of the sting on the near-wake structure, particularly the recirculation region, the separated shear layers, and the expansion/recompression process. Analysis of the unsteady base pressure field shows the presence of the sting suppresses dynamics that occur in the no-sting cases. A modal decomposition of the near-wake velocity field suggests the behavior of the recirculation region is associated with the suppression of these dynamics.

*Keywords:* Unsteady Flows, High-Speed Wakes, Turbulence Modeling.

## 1 Introduction

High-speed wake flows have generated significant interest over the years due to the fundamental complexity of the flowfield, as well as their relation to numerous practical applications. The separated shear layers are perhaps the signature fluid dynamic construct of this complex, three-dimensional, compressible turbulent flow, and their dynamics affect the expansion/recompression process, along with the recirculating flow near the base. These unsteady phenomena can have a significant influence on quantities of practical interest to designers, such as drag and unsteady loading, thus understanding their dynamics are critical for creating efficient, reliable vehicles.

The dynamics of these flows have been examined using experimental, computational, and theoretical approaches. An extensive experimental campaign was performed at the University of Illinois to characterize the fundamental fluid dynamics of a Mach 2.49 cylinder wake, particularly regarding the base pressure unsteadiness [1], near-wake turbulence statistics [2], and coherent structure dynamics [3]. This flow has also been studied computationally, with multiple researchers noting the difficulty of predicting these flows using Reynolds-Averaged Navier-Stokes (RANS) approaches [4, 5, 6], and the importance of properly resolving the incoming boundary layers to correctly predict the wake dynamics [7, 8]. The combination of the extensive experimental data and the known requirements for accurately computing this flow renders it a prime candidate for this study.

Although a breadth of other insightful experimental [9, 10, 11, 12] and computational [13, 14, 15, 16] studies have been carried out on wakes, there are a finite number of computations and experiments that can be performed to characterize all quantities of interest throughout flight, thus designers often leverage simplified models informed by their data. One common quantity of interest is the amplitude of the base pressure fluctuations, which is most simply characterized by their root-mean-square (RMS) [17, 18]. However,

to obtain a more complete representation of the unsteady base pressure loading, the base pressure RMS is often utilized in conjunction with a power spectral density (PSD) model to describe the spectral content of the base pressure fluctuations [19, 20]. Although these models are valuable, there are limited datasets that examine these quantities at hypersonic conditions.

To address this, experiments were performed in the Sandia Hypersonic Wind Tunnel (HWT) to characterize the wake dynamics behind a sharp cone ($5^o$ half-angle) in a Mach 8 flow. One quantity of interest from these experiments was the unsteady base pressure fluctuations. However, when comparing the RMS of these fluctuations to theoretical models, the experimental values exhibit a noticeable reduction (see cross symbol in Fig. 1). One possible rationale for this discrepancy is how the cone was mounted in the experiment. As shown in Fig. 2, the sting is located at the base of the cone, and is offset from the cylinder axis (this configuration is denoted the 'offset-sting' case). It was then conjectured that the presence of this sting influenced the near-wake dynamics in a non-insignificant manner, thereby inspiring the present study.

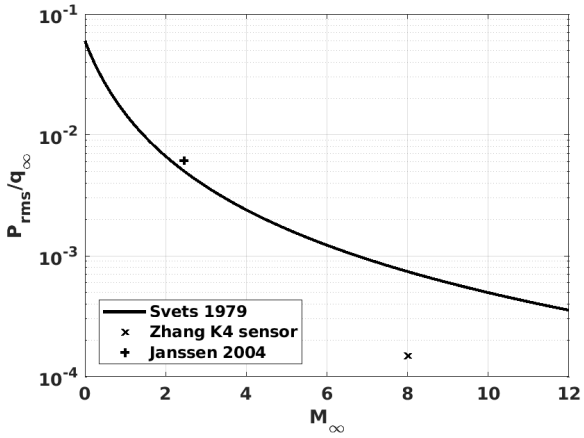


Figure 1: Comparison of $P_{rms}/q_\infty$ between experiment and theory. The variables $q_\infty$ and $M_\infty$ denote the freestream dynamic pressure and the freestream Mach number.

The goal of this work is to assess the influence of stings on near-wake unsteadiness using high-fidelity, scale-resolving simulations. Three sting configurations are considered; a 'centered-sting' configuration (where the sting axis is aligned with the body axis), an 'offset-sting' configuration (where the sting axis is *not* aligned with the body axis), and a 'no-sting' configuration. These three sting configurations are simulated on the Mach 8 sharp cone wake, as well as the Mach 2.49 cylinder wake. Simulation results are used to assess the influence of the sting on the near-wake unsteadiness, as well as identify the prominent physical phenomena.

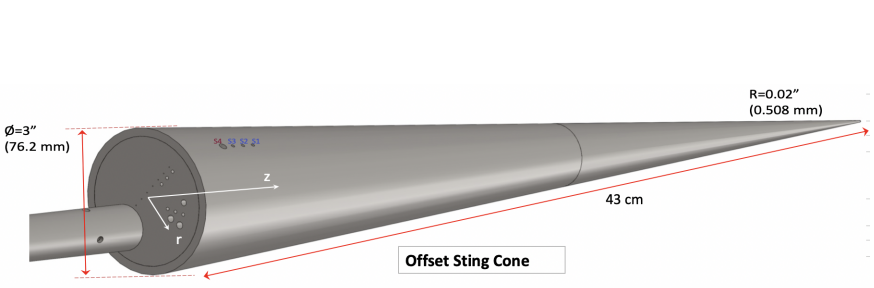


(a) Three-dimensional view

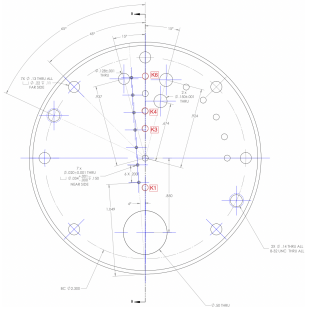

(b) Kulite locations

Figure 2: Geometrical representation of the offset-sting $5^o$ half-angle sharp cone experiment.

The rest of the paper is organized as follows. The simulation methodology, problem definition, and pertinent flowfield and geometrical parameters are described in Section 2. Results of the study are presented

in Section 3, beginning with a qualitative comparison to experimental data (Section 3.1), followed by an examination of the flow structure for each respective case (Section 3.2). The base pressure unsteadiness is explored in Section 3.3, with specific emphasis on the base pressure fluctuation RMS, and spectral content as a function of space. Lastly, connections between the base pressure field and the near-wake velocity field are derived from a modal decomposition of the velocity field in Section 3.4.

# 2 Problem Statement

To accurately replicate the cone and cylinder wake experiments, wall-modeled Large-Eddy Simulations are performed using the Sandia Parallel Aerodynamics and Re-entry Code (SPARC), which solves the full unsteady, compressible, finite volume representation of the three-dimensional Navier-Stokes equations. In this work, time-integration is performed using a $2^{\text{nd}}$-order implicit method, inviscid fluxes are discretized using the low-dissipation $4^{\text{th}}$-order scheme of Subbareddy and Candler [21], viscous fluxes are treated with a $2^{\text{nd}}$-order scheme, and wall-modeling is performed using an algebraic equilibrium wall-stress function. Additional dissipation is introduced through a numerical means by blending the low-dissipation $4^{\text{th}}$-order flux with a $2^{\text{nd}}$-order Steger-Warming flux [22], where the blending is controlled by the Larsson dissipation switch [23]. Additionally, to accurately reproduce the turbulent boundary layer present in experiments, the inflow plane is seeded with an incoming turbulent boundary layer generated by the synthetic digital filtering method (SDFM) of Adler *et al.* [24]. The statistics required to initialize the SDFM were obtained from a precursor RANS simulation. For the cases of interest, experience has demonstrated that placing the inflow plane 20 incoming boundary layer thicknesses ($\delta_0$) upstream of the base allows for sufficient relaxation of the inflow turbulence to an equilibrium state. Additional details regarding SPARC, including code design, supported physics, performance scaling, and verification can be found in [25, 26].

Experimental measurements were carried out in the Sandia HWT, which is a conventional blowdown-to-vacuum facility with an interchangeable system of nozzles and heater sections that allow operation at either Mach 5, 8, or 14. In this work, only Mach 8 was used. During Mach 8 operation, nitrogen is the freestream gas, and the total temperature and pressure ranges of the facility allow a freestream unit Reynolds number between 3.3 and $20 \times 10^6/m$. Base pressure measurements were taken using Kulite Mic-062 sensors sampled at $500kHz$, and whose signals were low-pass filtered from $100Hz$ to $20kHz$.

A summary of relevant flow and geometrical parameters for each case is provided in Table 1. Regarding the freestream conditions (denoted by the $\infty$ subscript), the cone conditions correspond to the incoming flow to the body, whereas for the cylinder wake, these conditions represent the incoming flow to the base. As for the geometrical parameters, the base diameter is denoted by $D$, the sting diameter is represented by $D_s$, and the offset distance of the sting axis from the body axis is designated $d_o$. Throughout this work, the $x$-direction is defined as the streamwise coordinate, and the sting is displaced in the $y$-direction, thus for all cases, an $x$-$y$ plane located at $z = 0$ is representative of a symmetry plane. To maintain consistency between the sting diameters and offset displacements between the cone and cylinder cases, the ratios $D/D_s$ and $D/d_o$ are kept constant, with the ratios being chosen in accordance with the cone experiments. All simulations take into account the full three-dimensionality of the geometry, and for the sting cases, the sting extends to the end of the computational domain. Grid densities for the wall-modeled turbulent boundary layer upstream of the base are derived from the suggestions of Kawai and Larsson [27], while near-wake grid densities were chosen based on experience. These densities result in grids containing $83 \times 10^6$ and $183 \times 10^6$ nodes for the no-sting cylinder and no-sting cone cases respectively.

| Case | $\rho_\infty (kg/m^3)$ | $u_\infty (m/s)$ | $T_\infty (K)$ | $\delta_0$ (mm) | Gas | $D$ (mm) | $D_s$ (mm) | $d_o$ (mm) |
|---|---|---|---|---|---|---|---|---|
| Cone | 0.04215 | 1085.45 | 44.27 | 3.4 | Nitrogen | 76.2 | 24.1 | 21.0 |
| Cylinder | 0.6482 | 565 | 128.63 | 3.5 | Air | 63.5 | 20.1 | 18.0 |

Table 1: Relevant flow and geometrical parameters.

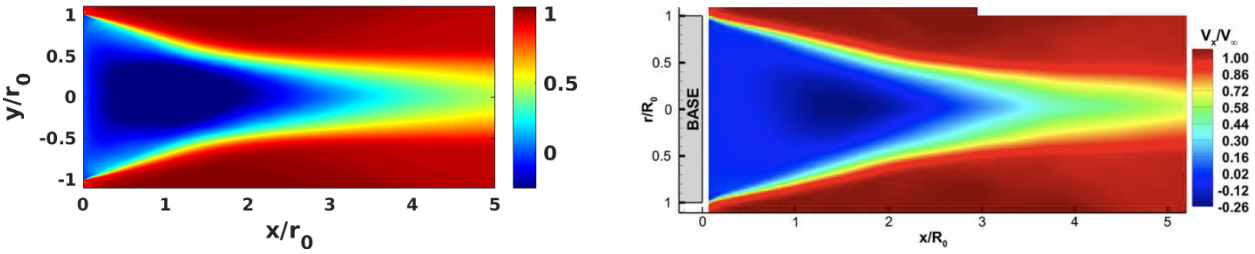


(a) Simulation

(b) Experiment [2]

Figure 3: Comparison of the mean $u/u_\infty$ for the no-sting cylinder case.

# 3 Results

## 3.1 Comparison to Experiment

This section begins with a qualitative comparison between simulation results and available experimental data. A comparison of the mean streamwise ($u$) velocity field for the no-sting cylinder case and the experiment of Kirchner *et al.* [2] is shown in Fig. 3. First, it is important to note that both plots have the $u$-velocity normalized by the freestream velocity ($u_\infty$), and that the spatial coordinates have been normalized by the radius of the base ($r_0$). This spatial normalization will be commonplace throughout the remainder of this work. This figure shows the simulation reproduces the structure of the mean $u$-velocity field quite well, particularly in terms of the wake length, as the blue region in both the simulation and experiment terminates near $x/r_0 = 3.5$. Additionally, the simulation captures the transition of the attached turbulent boundary layer to diffuse, separated shear layers. However, there are a few subtle differences. One such difference is observed at $x/r_0 = 5$, where the simulation exhibits an increased vertical extent of the wake compared to the experiment, indicating slightly different growth rates of the separated shear layer during the expansion/recompression process. Furthermore, simulation results display a saturation of the blue contours in the recirculation region near the base, suggesting that there is a larger magnitude and spatial extent of reverse flow. This phenomenon has also been observed in the computations of Simon *et al.* [8]. Comparisons of the remaining sting-based cases for the cylinder are not available due to the lack of experimental data. However, these results provide confidence in this modeling approach for the sting-based cylinder cases.

A comparison of the flow structure between simulation and experiment is now performed for the centered-sting and offset-sting cone cases. The centered-sting flowfields are shown in Figs. 4a-4b, and the offset-sting flowfields are shown in Figs. 4c-4d. Note that unlike other flow visualizations throughout the paper, in effort to be consistent with the experiment, the flow direction of the simulation is from right to left. From initial observation, the simulations exhibit a favorable comparison to experiment. The simulation clearly captures the overall features of the complex separation/reattachment dynamics of the separated shear layer, and exhibits a similar increase in wake size above the sting for the offset-sting case. Comparing the angle between the recompression wave and the sting axis indicates the simulations and experiment compare fairly well. Discrepancies between the angles could be associated with the inherent error in computing this quantity. For the offset-sting simulation, the vertical height of the wake above the sting is approximately $1.25in.$, which is comparable to the experimental value of $1.4in.$, thereby providing further confidence in the simulation results. However, it is important to note that some of these discrepancies between simulation and experiment could be a result of Reynolds number differences (see Fig. 4 insets). Regardless, the overall comparison to experiment is satisfactory for the purposes of this study, and similar to the cylinder, this comparison provides confidence in the ability to simulate the case without an experimental counterpart.

## 3.2 Instantaneous Flowfield

Realizations of the instantaneous $u$-velocity for each case are shown in Figs. 5 and 6. In all figures, the respective geometrical features are colored white, and the expansion/recompression process, as well as the turbulence within the various shear layers, is readily apparent. Comparing the no-sting cases to the centered-sting cases, it is clear that the wake lengths are relatively comparable. However, comparing these cases to

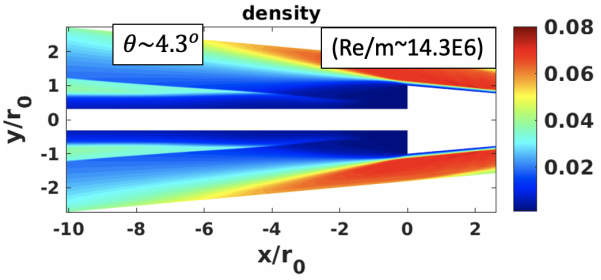


(a) Simulation: centered-sting mean density field on an $x$-$y$ plane at $z = 0$.

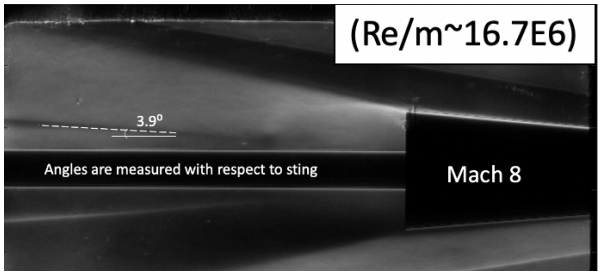


(b) Experiment: centered-sting mean Schlieren.

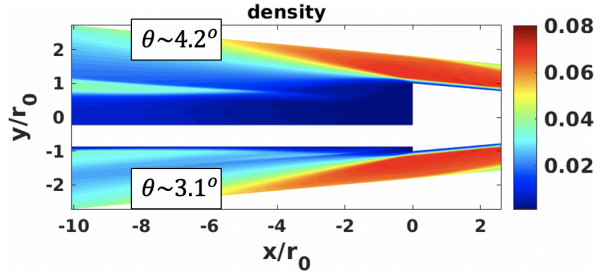


(c) Simulation: offset-sting mean density field on an $x$-$y$ plane at $z = 0$.

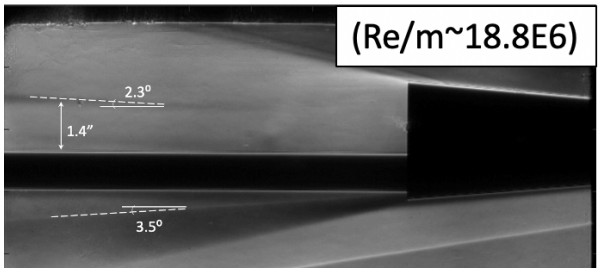


(d) Experiment: offset-sting mean Schlieren.

Figure 4: Comparison of the mean flowfield for sting-based cone cases. The flow direction is from right to left, and the Reynolds number for each respective case is given in the inset.

the offset-sting cases, there are both similarities and differences. The similarities are present in the $x$-$z$ plane, where the wake size and downstream wake structure are comparable, but in the $x$-$y$ plane, there is an apparent lengthening of the wake and increased size of the low-velocity region in the upper portion of the wake. Comparing the cylinder cases to the cone cases, there is a noticeable absence of fine-scale structures in the recirculation region for the cone cases. A detailed grid-resolution study (not shown here) demonstrated that refining the cone grid in the near-wake region, resulting in a grid containing approximately $613 \times 10^6$ nodes, produced a negligible difference in the fine-scale structures in the recirculation region, along with minimal variations in velocity field statistics and base pressure unsteadiness. The lack of fine-scale structures in the circulation region of the cone wake could be a result of the known association between increased compressibility and a reduction of shear layer instability growth rates [28], or the reduced Reynolds number compared to the cylinder.

### 3.3 Base Pressure Unsteadiness

The investigation of the base pressure unsteadiness begins with the RMS levels as a function of the distance ($d$) from the body axis (Fig. 7). In this figure, 'NS' denotes a no-sting case, 'CS' denotes a centered-sting case, and 'OS' denotes an offset-sting case. The arrays within these plots are positioned at the base locations depicted in Figs. 5 and 6, where 'OS Z-L' represents the data extracted from an $x$-$y$ plane at $z = 0$ at locations above the sting, 'OS Z-S' represents the equivalent data located below the sting, and 'OS Y' represents the data extracted from an $x$-$z$ plane at $y = 0$. From these plots, it is clear that the sting-based cases show a reduction in base pressure fluctuation amplitude compared to the no-sting cases. There are several additional details about these plots that are important to note. First, the largest fluctuation amplitude for the no-sting cases is observed near the body axis, suggesting that the recirculation region dynamics, which are inherently tied to the separated shear layers, play a significant role in the overall amplitude of the base pressure unsteadiness. Second, there is an apparent three-dimensionality in the base pressure fluctuation RMS for the offset-sting cylinder case that is not present for the offset-sting cone case. For all sting-based cone cases, the RMS is relatively constant in space. However for sting-based cylinder cases, there is a notable spatial

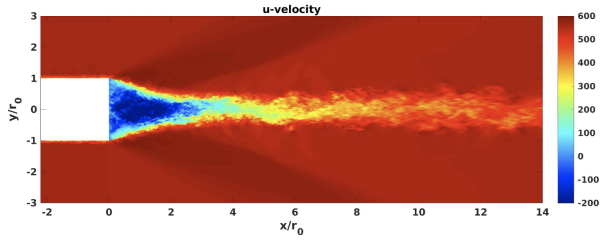


(a) No-sting

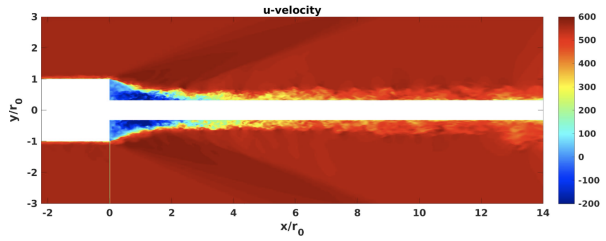


(b) Centered-sting

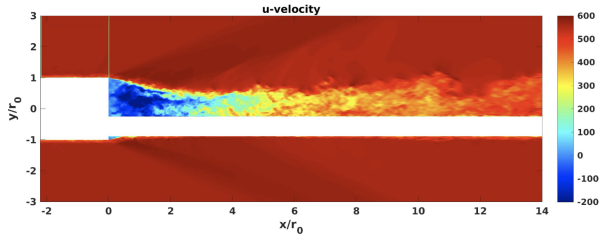


(c) Offset-sting, $x$-$y$ plane at $z = 0$

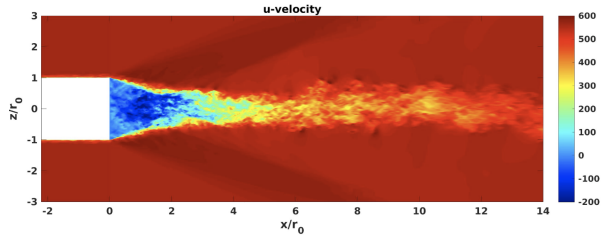


(d) Offset-sting, $x$-$z$ plane at $y = 0$

Figure 5: Realizations of the instantaneous $u$-velocity for the cylinder cases.

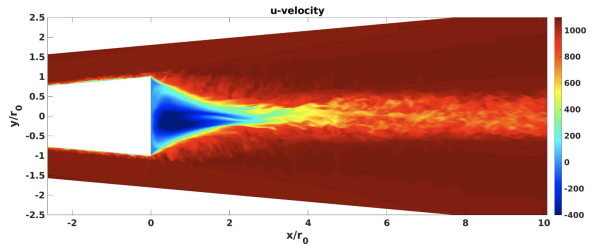


(a) No-sting

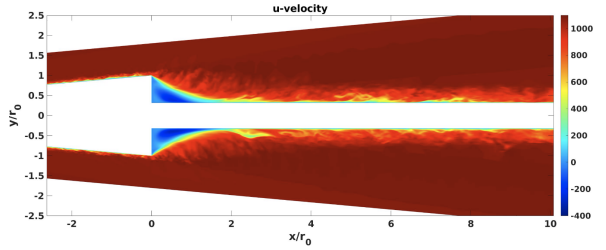


(b) Centered-sting

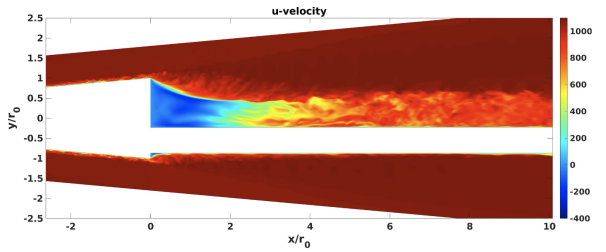


(c) Offset-sting, $x$-$y$ plane at $z = 0$

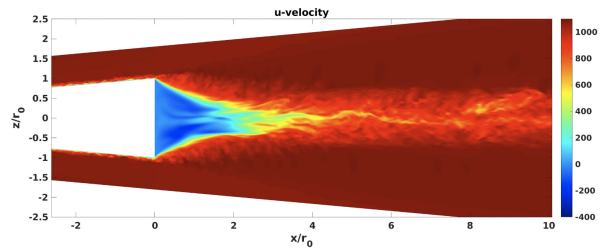


(d) Offset-sting, $x$-$z$ plane at $y = 0$

Figure 6: Realizations of the instantaneous $u$-velocity for the cone cases.

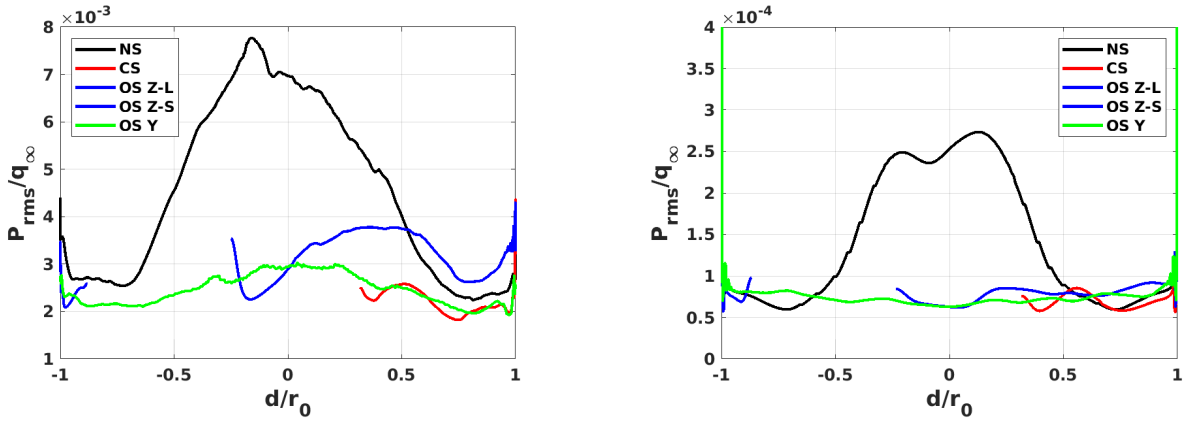


(a) Cylinder (b) Cone

Figure 7: Plots of $P_{rms}/q_\infty$ as a function of the normalized distance from the body axis. 'NS', 'CS', and 'OS' denote the no-sting, centered-sting, and offset-sting cases respectively.

variation of RMS levels. Specifically, 'OS Z-L' exhibits a larger peak RMS than 'OS Y', indicating a possible connection between the recirculation region size and the base pressure fluctuation amplitude. Additionally, it is noted that the spatial trend of 'OS Y' follows that of 'NS', albeit at a much lower amplitude.

A comparison of the base pressure fluctuation RMS values between simulation results and available experimental data is shown in Fig. 8, where it is clear that the presence of a sting has an influence on the overall base pressure fluctuation magnitude. For the cylinder, it is encouraging that the simulation, experiment, and theoretical value are in good agreement with each other. With the cone, although the direct comparison between the K4 sensor in the experiment (see Fig. 2b) and the offset-sting case is not as good as the cylinder, the general trend of the sting reducing the fluctuation amplitude is apparent. Comparing the no-sting cone case to the theoretical value, it is unclear whether the inconsistency is caused from modeling errors on the simulation side, or modeling assumptions on the theoretical side. However, as consistent with the theory, both simulation and experiment clearly exhibit a reduction in base pressure fluctuation amplitude with increasing freestream Mach number.

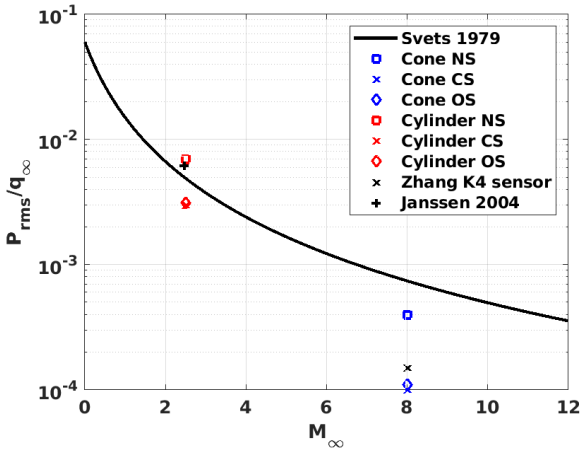


Figure 8: Comparison of $P_{rms}/q_\infty$ between computations, experiment, and theory.

To assess the spectral content of the base pressure fluctuations, their premultiplied power spectral density (PPSD) is now examined. In effort to more strictly compare the spectral content between different locations on the base, the PPSD has been normalized such that the PPSD at each spatial location has unit energy.

The normalized PPSD of the base pressure fluctuations are shown in Fig. 9, with the $y$-axis of the plots denoting the normalized spatial location, the $x$-axis denoting the Strouhal number constructed using the base diameter and freestream velocity, and the white regions corresponding to the sting location. For reference, a Strouhal number of unity corresponds to approximately $14kHz$ and $9kHz$ for the cone and cylinder cases respectively. Beginning with the no-sting cases (Figs. 9a-9b), the spectra show that, as consistent with other studies [1, 20], the region near the body axis is dominated by low-frequency unsteadiness ($St_D < 0.25$). Furthermore, it was shown previously that the highest-amplitude base pressure fluctuations occur near the body axis, thus these results provide evidence that these high-amplitude fluctuations are associated with low-frequency unsteadiness. However, away from the body axis, the prominent frequencies transition to larger values ($St_D > 1$), which are likely associated with separated shear layer unsteadiness. Interestingly, all of the sting-based cases (Figs. 9c-9h) exhibit negligible amounts of the low-frequency unsteadiness that was evident near the body axis for the no-sting cases, thereby suggesting that the presence of the sting suppresses the dynamics associated with these frequencies. The physical mechanisms that are likely associated with these frequencies are discussed next.

### 3.4 Near-Wake Velocity Field Unsteadiness

The near-wake velocity field is now analyzed in effort to connect its dynamics to the base pressure unsteadiness. To identify the large-scale coherent structures commonly associated with turbulent wakes [3, 14, 29, 30], the near-wake velocity field is decomposed into orthogonal basis functions (*i.e.* modes) using the snapshot method of proper orthogonal decomposition (POD) originally proposed by Sirovich [31]. With this approach, $N$ snapshots of the velocity field is first subjected to the classical Reynolds decomposition ($u_i = \bar{u_i} + u_i'$), then the fluctuating component is further decomposed to a collection of spatial modes ($\phi$) and temporal coefficients ($a$), such that performing a summation over the temporal coefficients and spatial modes reconstructs the fluctuating component:

$$u_i'(\mathbf{x}, t) = \sum_{j=1}^{N} a_j(t)\phi_j(\mathbf{x}). \tag{1}$$

The resulting modes are sorted by decreasing energy contribution, with mode 1 containing the most energy. To account for the full turbulent kinetic energy within the wake, this decomposition is performed using all three velocity components. Lastly, the decomposition is carried out using 3000 snapshots of an $x$-$y$ plane at $z = 0$ sampled at $200kHz$ ($St_D \sim 14$), corresponding to $15ms$ of physical time.

Results are presented here for the no-sting and centered-sting cone cases only, as the offset-sting cone case exhibited many similarities to the centered-sting cone case, and the cylinder cases displayed comparable dynamics to the respective cone case counterpart. Figure 10 shows the leading mode shapes for the $u$ and $v$-velocity components, along with the corresponding PPSD of the temporal coefficients for the no-sting cone case. The leading mode corresponds to a 'pulsating' motion of the wake [32], while the second mode seemingly describes a large-scale flapping-like motion of the separated shear layers. As observed in Fig. 10f, the frequencies associated with the temporal coefficients of these leading two modes is consistent with the low-frequency unsteadiness observed in the base pressure PPSD (see Fig. 9a). While the remaining modes are also connected with shear layer unsteadiness, these modes appear to describe a dynamical coupling between the shear layers and the recirculation region. Additionally, the temporal coefficients of these modes also contain the low-frequency content observed in the base pressure PPSD, thereby highlighting the connection between the low-frequency unsteadiness of the separated shear layers, recirculation region, and base pressure.

POD results for the centered-sting cone case are presented in Fig. 11. Similar to the no-sting case, the leading two modes of the centered-sting case (Figs. 11a- 11b) correspond to a pulsating motion of the wake, and a large-scale flapping-like motion of the separated shear layers. Interestingly, the frequencies associated with these modes are also consistent with that of the low-frequency base pressure unsteadiness observed in the no-sting case, however as observed in the centered-sting base pressure PPSD (see Fig. 9c), these frequencies are not prominent. A possible rationale for the absence of low-frequency unsteadiness in the centered-sting base pressure spectra, even though the dominant POD modes are associated with these frequencies, is discussed below. As for the remaining centered-sting POD modes (Figs. 11c- 11e), each mode describes large-scale structures initiated from the separated shear layer that persist for a much further streamwise extent than the structures in the no-sting case, and as observed from the PPSD of the temporal coefficients,

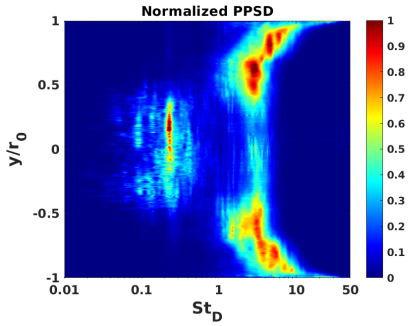


(a) Cone: NS

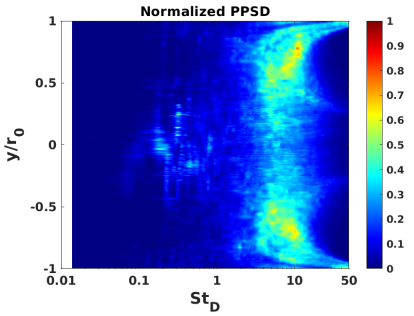


(b) Cylinder: NS

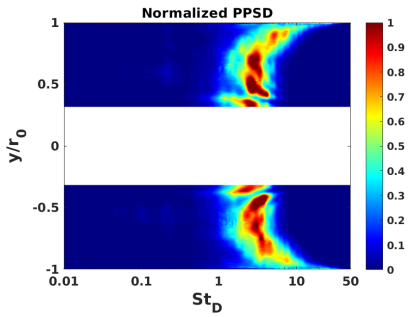


(c) Cone: CS

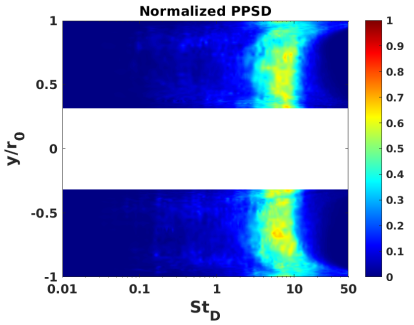


(d) Cylinder: CS

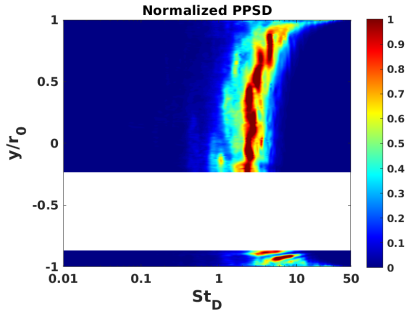


(e) Cone: OS, $x$-$y$ plane at $z = 0$

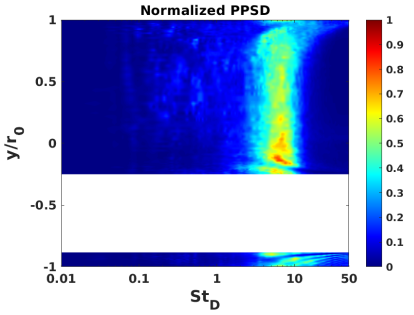


(f) Cylinder: OS, $x$-$y$ plane at $z = 0$

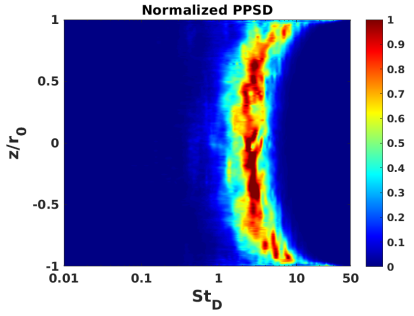


(g) Cone: OS, $x$-$z$ plane at $y = 0$

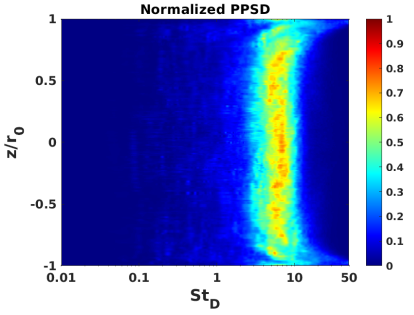


(h) Cylinder: OS, $x$-$z$ plane at $y = 0$

Figure 9: Contour plots of the normalized premultiplied power spectral density (PPSD) as a function of radial distance. Cone cases are in the left column, and cylinder cases are in the right column. The nondimensional frequency ($St_D$) is based on the respective base diameter and the freestream velocity. The white regions correspond to the sting location.

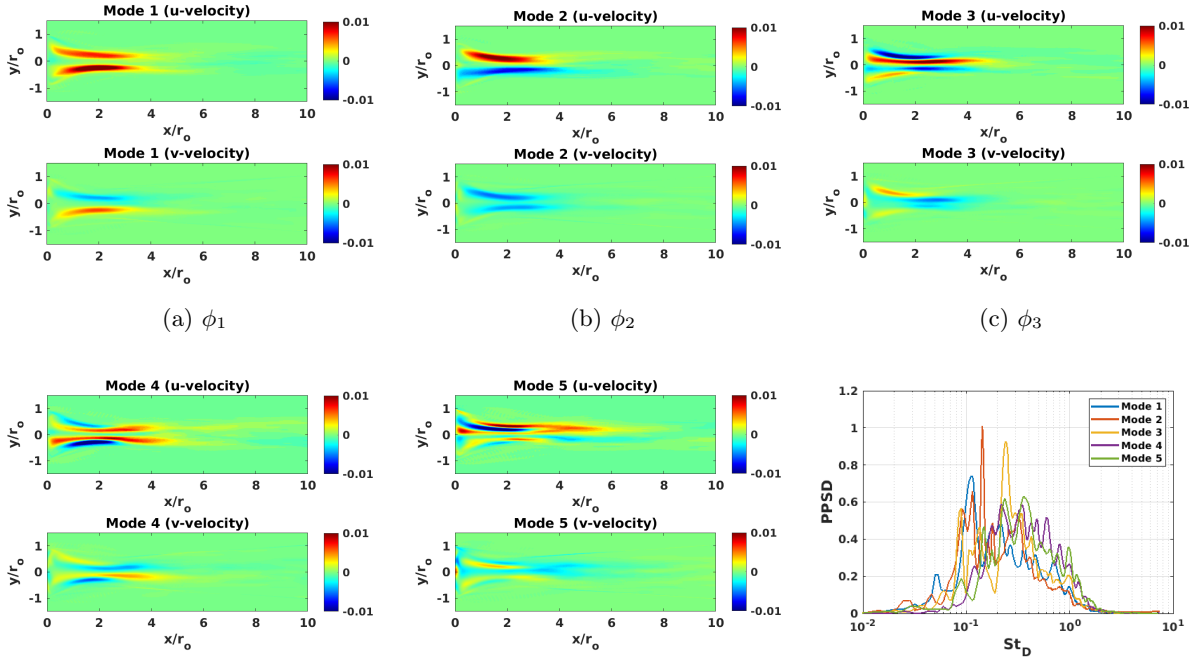


(a) $\phi_1$ (b) $\phi_2$ (c) $\phi_3$

(d) $\phi_4$ (e) $\phi_5$ (f) Normalized PPSD of the temporal coefficients.

Figure 10: POD results for the no-sting cone case.

these modes also contain the low-frequency content observed in the no-sting base pressure spectra.

It is perplexing that the dominant flow structures for the centered-sting case contain low-frequency unsteadiness that is not manifested in the base pressure unsteadiness in the same manner as the no-sting case. Focusing on the recirculation region, it is clear that the POD modes of the no-sting case are associated with unsteadiness in this region, whereas in the centered-sting case, the dominant POD modes are not significantly associated with unsteadiness in this region. Through the coupling of the pressure and velocity fields, it can be reasoned that the recirculation region unsteadiness in the no-sting case, particularly that observed in Figs. 10c-10e, is associated with the low-frequency unsteadiness of the base pressure field near the body axis. These results suggest that the effect of the sting is to suppress the unsteadiness of the recirculation region, which in turn affects the base pressure field unsteadiness. Furthermore, the fact that the presence of the sting allows large-scale structures to persist further downstream indicates reduced mixing of the wake, which is likely associated with the no-slip condition preventing cross-wake mixing by large-scale structures. These results show the sting significantly influences the near-wake velocity field unsteadiness, whose dynamics intrinsically influence the base pressure field.

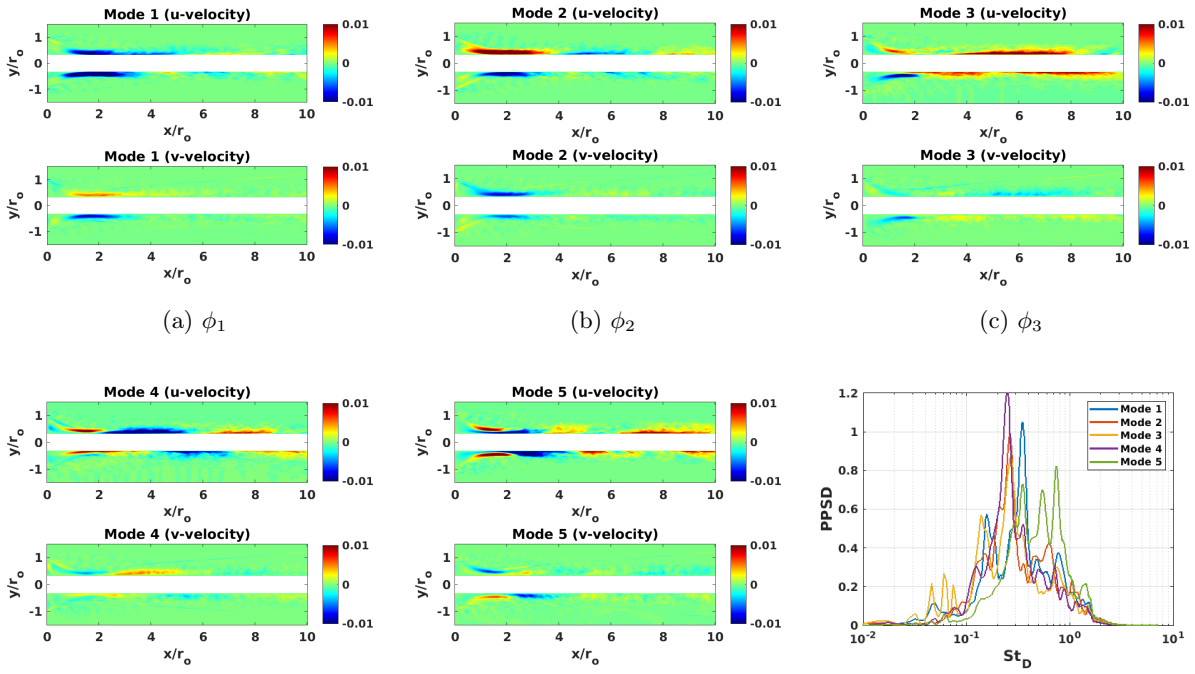


(a) $\phi_1$ (b) $\phi_2$ (c) $\phi_3$

(d) $\phi_4$ (e) $\phi_5$ (f) Normalized PPSD of the temporal coefficients.

Figure 11: POD results for the centered-sting cone case.

# 4 Conclusion and Future Work

Wall-modeled large-eddy simulations were performed to assess the influence of blunt body base protuberances (*i.e.* a sting) on the unsteadiness of a Mach 2.49 cylinder wake and a Mach 8 cone wake. For both of these flows, three different sting configurations were simulated; namely a 'no-sting' case, a 'centered-sting' case, and an 'offset-sting' case. Comparisons of simulation results with available experimental data were favorable, thereby providing confidence in the simulation fidelity for the quantities of interest. The presence of the sting was shown to dramatically influence the near-wake structure, particularly in terms of the separated shear layer and the associated expansion/recompression process, along with the recirculation region. Inclusion of the sting was shown to reduce the overall amplitude of the base pressure fluctuations, and suppress the low-frequency unsteadiness observed in the no-sting cases. Proper orthogonal decomposition of the near-wake velocity field for select cases highlighted large-scale coherent structures with similar low-frequency content as the base pressure spectra in the no-sting cases. However when a sting was present, the unsteady dynamics observed in the recirculation region near the base was diminished, thereby providing a potential mechanism to explain the suppression of the low-frequency base pressure fluctuations for sting-based cases.

# Acknowledgements

Sandia National Laboratories is a multimission laboratory managed and operated by National Technology and Engineering Solutions of Sandia, LLC, a wholly owned subsidiary of Honeywell International Inc., for the U.S. Department of Energy's National Nuclear Security Administration under contract DE-NA0003525.

# References


[1] J. R. Janssen and J. C. Dutton. Time-Series Analysis of Supersonic Base-Pressure Fluctuations. *AIAA Journal*, 42(3), March 2004.

[2] B. K. Kirchner, J. V. Favale, G. S. Elliot, and J. C. Dutton. Three-Component Turbulence Measurements and Analysis of a Supersonic, Axisymmetric Base Flow. *AIAA Journal*, 57(6), June 2019.

[3] B. M. Kirchner, G. S. Elliot, and J. C. Dutton. Coherent turbulence and entrainment in a supersonic, axisymmetric, separated/reattaching shear layer. *Physical Review Fluids*, 5(084605), August 2020.

[4] P. K. Tucker and W. Shyy. A Numerical Analysis of Supersonic Flow over an Axisymmetric Afterbody. *AIAA Paper 93-2347*, June 1993.

[5] J. L. Papp and K. N. Ghia. Application of the RNG Turbulence Model to the Simulation of Axisymmetric Supersonic Separated Base Flow. *AIAA Paper 2001-0727*, January 2001.

[6] J. R. Forsythe, K. A. Hoffmann, R. M. Cummings, and K. D. Squires. Detached-Eddy Simulation with Compressibility Corrections Applied to a Supersonic Axisymmetric Base Flow. *Journal of Fluids Engineering*, 124:911–923, 2002.

[7] S. Kawai and K. Fujii. Computational Study of Supersonic Base Flow Using Hybrid Turbulence Methodology. *AIAA Journal*, 43(6), June 2005.

[8] F. Simon, S. Deck, and P. Guillen. Reynolds-Averaged Navier-Stokes/Large-Eddy Simulations of Supersonic Base Flow. *AIAA Journal*, 44(11), November 2006.

[9] M. Braza, R. Perrin, and Y. Hoarau. Turbulence properties in the cylinder wake at high reynolds numbers. *Journal of Fluids and Structures*, 22:757–771, 2006.

[10] R. A. Humble, F. Scarano, and B. W. van Oudheusden. Unsteady flow organization of compressible planar base flows. *Physics of Fluids*, 17, 2007.

[11] D. M. Moore, C. W. Letchford, and M. Amitay. Energetic scales in a bluff body shear layer. *Journal of Fluid Mechanics*, 875:543–575, 2019.

[12] M. Viji and N. S. Vikramaditya. Modes of Base Pressure Fluctuations: Shape, Nature, and Origin. *AIAA Journal*, 57(9), September 2019.

[13] G. Karniadakis and G. S. Triantafyllouw. Three-dimensional dynamics and transition to turbulence in the wake of bluff objects. *Journal of Fluid Mechanics*, 238:1–30, 1992.

[14] X. Ma, G. Karamanos, and G. Karniadakis. Dynamics and low-dimensionality of a turbulent near wake. *Journal of Fluid Mechanics*, 410:29–65, 2000.

[15] J. M. Brock, P. K. Subbareddy, and G. V. Candler. Detached-Eddy Simulations of Hypersonic Capsule Wake Flow. *AIAA Journal*, 53(1), January 2015.

[16] W. S. Hinman and C. T. Johansen. Reynolds and Mach Number Dependence of Hypersonic Blunt Body Laminar Near Wakes. *AIAA Journal*, 55(2), February 2017.

[17] L. E. Chaump, A. Martellucci, and A. Montfort. Aeroacoustic Loads Associated with High Beta Re-Entry Vehicles. Technical report, AFFDL-TR-72-138, 1973.

[18] A. I. Shvets. Base Pressure Fluctuations. *Fluid Dynamics*, 14(3):394–401, 1979.

[19] A. Goldburg, W. K. Washburn, and B. H. Florsheim. Strouhal numbers for the hypersonic wakes of spheres and cones. *AIAA Journal*, 3(7), 1965.

[20] L. J. DeChant and J. L. Smith. An Approximate Expression for Base Pressure Fluctuation Spectra for Bluff Bodies. In *49th AIAA Aerospace Sciences Meeting*, 2011.

[21] P. K. Subbareddy and G. V. Candler. A fully discrete, kinetic energy consistent finite volume scheme for compressible flows. *Journal of Computational Physics*, 28:1347–1364, 2009.

[22] J. L. Steger and R. F. Warming. Flux vector splitting of the inviscid gasdynamic equations with application to finite-difference methods. *Journal of Computational Physics*, 40:263–293, April 1981.

[23] J. Larsson, R. Vicquelin, and I. Bermejo-Moreno. Large Eddy Simulations of the HyShot II Scramjet. *Center For Turbulence Research, Annual Research Report Briefs*, 2011.

[24] M. C. Adler, D. R. Gonzalez, C. M. Stack, and D. V. Gaitonde. Synthetic generation of equilibrium boundary layer turbulence from modeled statistics. *Computers and Fluids*, 165:127–143, March 2018.

[25] M. Howard, T. Fisher, M. Hoemmen, D. Dinzl, J. Overfelt, A. Bradley, K. Kim, and S. Rajamanickam. Employing Multiple Levels of Parallelism for CFD at Large Scales on Next Generation High-Performance Computing Platforms. *ICCFD10*, 2018.

[26] B. A. Freno, B. R. Carnes, and V. G. Weirs. Code-verification techniques for hypersonic reacting flows

in thermochemical nonequilibrium. *Journal of Computational Physics*, 425, January 2021.

[27] S. Kawai and J. Larsson. Wall-modeling in large eddy simulation: Length scales, grid resolution, and accuracy. *Physics of Fluids*, 24:15105, 2012.

[28] D. Papamoschou and A. Roshko. The compressible turbulent shear layer: an experimental study. *Journal of Fluid Mechanics*, 197:453–477, December 1999.

[29] H. V. Fuchs, E. Mercker, and U. Michel. Large-scale coherent structures in the wake of axisymmetric bodies. *Journal of Fluid Mechanics*, 93:185–207, 1979.

[30] A. K. M. F. Hussain. Coherent structures and turbulence. *Journal of Fluid Mechanics*, 173:303–356, December 1986.

[31] L. Sirovich. Turbulence and the Dynamics of Coherent Structures Part 1: Coherent Structures. *Quarterly of Applied Mathematics*, 45(3):561–571, 1987.

[32] R. Humble, F. Scarano, and B. van Oudheusden. Unsteady Planar Base Flow Investigation Using Particle Image Velocimetry and Proper Orthogonal Decomposition. *44th AIAA Aerospace Sciences Meeting and Exhibit*, 2006.